Science Advances
AAAS

Supplementary Materials for

Broadband uniform-efficiency OAM-mode detector

Suman Karan *et al.*

Corresponding author: Suman Karan, karans@iitk.ac.in; Anand K. Jha, akjha@iitk.ac.in

Sci. Adv. **11**, eadq7201 (2025)
DOI: 10.1126/sciadv.adq7201

This PDF file includes:

Supplementary Sections S1 to S6
Figs. S1 to S5

1 Mode dependent detection efficiency in sigle-mode fiber-based measurement

Figure S1 shows the typical experimental setup for the single-mode fiber-based (SMF) OAM spectrum measurement *(25,26)* . The electric field of a Laguerre-Gaussian (LG) mode $LG_p^l(\rho,\phi)$ at the beam waist plane can be written as *(1)*

$$LG_p^l(\rho,\phi) = \sqrt{\frac{2\,p!}{\pi {w_0}^2\,(p+|l|)!}}\left(\frac{\rho\sqrt{2}}{w_0}\right)^{|l|} \exp\left[-\frac{\rho^2}{w_0^2}\right] L_p^{|l|}\left(\frac{2\rho^2}{w_0^2}\right) e^{-il\phi}, \tag{S1}$$

where l is an integer ranging from $-\infty$ to ∞ and is referred to as the OAM-mode index while p is called the radial-mode index, and it ranges from 0 to ∞. $L_p^l[\ldots]$ is called the associated Laguerre polynomial given by $L_p^l[x] = \sum_{m=0}^{p}(-1)^m \frac{(p+l)!}{(p-m)!(l+m)!}\frac{x^m}{m!}$ and w_0 is the beam waist of the field. The field amplitude $LG_p^l(\rho,\phi)$ can be written as a product of two separate parts, one containing the helical phase and the other containing the radial dependence: $LG_p^l(\rho,\phi) = LG_p^{|l|}(\rho)e^{-il\phi}$. For detecting this mode using an SMF, we need to first get rid

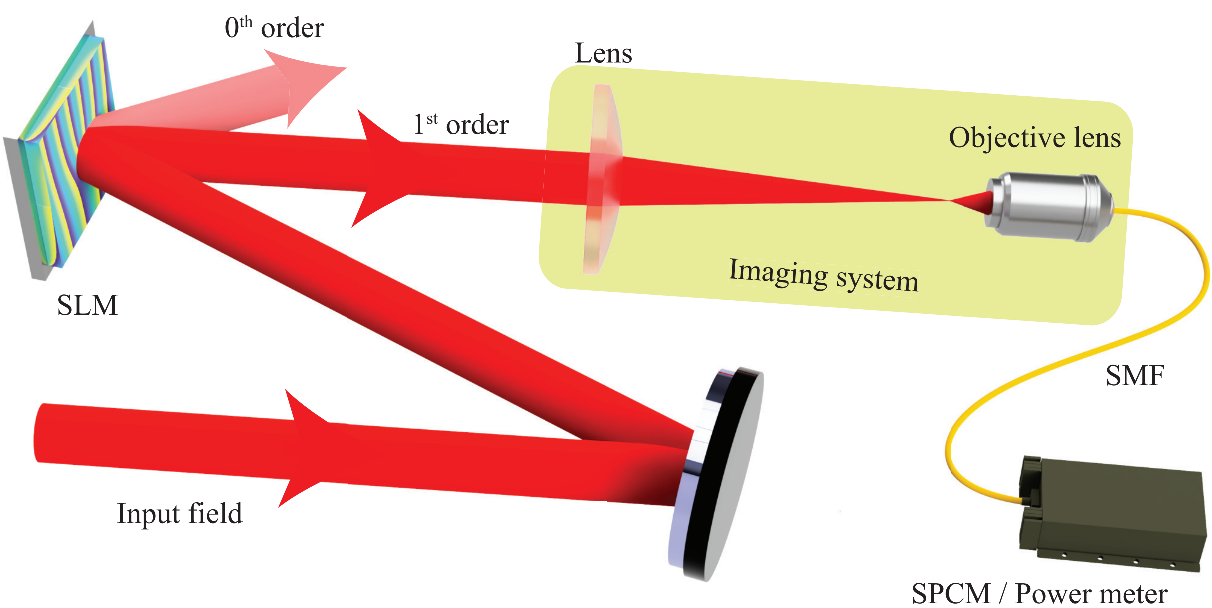

Figure S1: **Experimental setup for OAM mode detection using a spatial light modulator (SLM) and a single-mode fiber (SMF).** SPCM: single photon counting module.

of the helical phase $e^{-il\phi}$. For this, an additional complementary phase $e^{il\phi}$ is introduced by using a spatial light modulator (SLM). Next, as shown in Fig. S1, the first-order diffracted field from the SLM is coupled into the SMF of core radius $\sigma_{\rm smf}$ thorough a $4f$ lens configuration and collected either using a powermeter for high-light level measurement or using a single-photon counting module (SPCM) for single-photon counting. The SMF tip is imaged onto the SLM with a magnification factor of M. Therefore, the fundamental mode of the single-mode fiber (SMF) at the SLM plane can be written as

$$G(\rho) = \sqrt{\frac{2}{\pi\sigma^2}} e^{-\dfrac{\rho^2}{\sigma^2}}, \tag{S2}$$

where $\sigma = M\sigma_{\rm smf}$ is the mode radius at the SLM plane. Thus, the coupling-coefficient to the SMF for the input mode $LG_p^l(\rho,\phi)$ can be obtained by the following overlap integral

$$C_l^p = \int_{\rho=0}^{\infty} \int_{\phi=0}^{2\pi} LG_p^l(\rho,\phi) \left[e^{-il\phi}\right]^* \sqrt{\frac{2}{\pi\sigma^2}} e^{-\rho^2/\sigma^2} \rho d\rho d\phi. \tag{S3}$$

The magnitude $|C_l^p|^2$ is taken as the coupling efficiency. In practical experimental situations, the first order diffraction efficiency of the SLM and the quantum efficiency of the detectors (SPCM/powermeter) are never perfect, and as a result, the overall quantum efficiency of the detection system κ is always less than 1. The detection efficiency of the system for an LG mode can be defined as $\eta_l^p = \kappa |C_l^p|^2$, and after evaluating the overlap integral above, one can obtain the following expression for the detection efficiency η_l^p:

$$\eta_l^p = \kappa \frac{4\pi(p+|l|)!}{2^{|l|}p!} \left(\frac{w_0}{\sigma}\right)^2 \left| \left[\frac{(1+\frac{w_0^2}{\sigma^2})^{-1-|l|/2}}{\Gamma\left(\frac{|l|+1}{2}\right)} \right] 2F1 \left[-p, 1+\frac{|l|}{2}, 1+|l|, \frac{2}{1+\frac{w_0^2}{\sigma^2}} \right] \right|^2. \tag{S4}$$

Here $2F1[\ldots]$ represents the Gaussian hypergeometric function. In Fig. S2A we plot η_l^0/κ as a function of the OAM mode index $|l|$, for various σ/w_0 values. We find that the detection efficiency of the SMF-based detector is highly dependent on the OAM mode index $|l|$ and the ratio σ/w_0. The detection efficiency decreases very sharply with $|l|$, and as a result, the range of

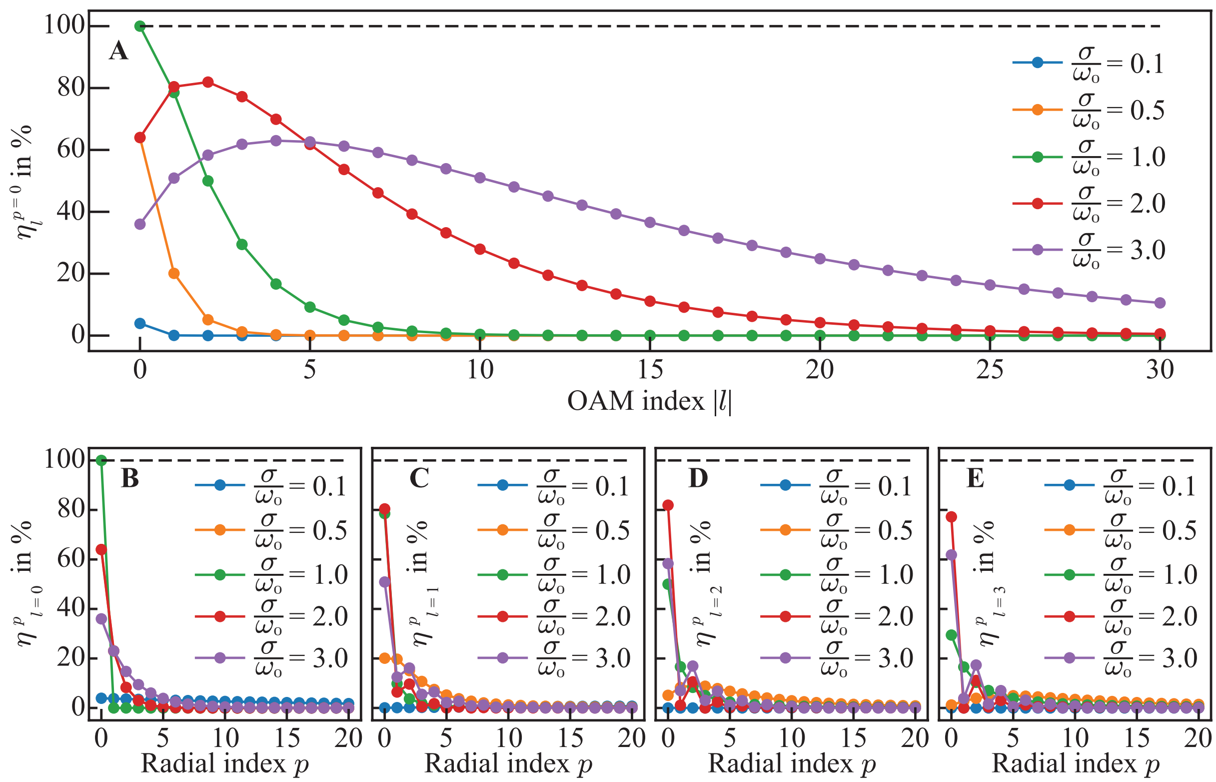

Figure S2: **Coupling efficiency as a function of OAM mode index l and radial mmode index p for five different values of the ratio σ/w_0.** **(A)** Plot of the coupling efficiency η_l^0 as a function of l. **(B-E)** Plots of η_l^p as a function of p for $l = 0$, $l = 1$, $l = 2$, and $l = 3$, respectively.

modes that can be detected with this detector is very small. Although this range can be increased by increasing σ/w_0, it leads to decrease in the overall efficiency of the detector. Figures. S2 B-S2E, show the plots of η_l^p/κ as a function of the radial mode index p for various l and σ/w_0. We find that η_l^0/κ is mostly maximum for $p = 0$ mode. Thus, we see that the SMF-based OAM detectors can primarily detect $p = 0$ mode, and even for this mode, these detectors have non-uniform detection efficiency and work for only a small range of OAM modes.

One might be inclined to think that by appropriately correcting for the fiber coupling efficiency, one can achieve uniform detection efficiency with an SLM-based OAM detector. However, we find that this may be possible to some extent, if one has the prior information that the spectrum-to-be-measured contains only $p = 0$ modes. However, if the unknown state contains

$p \neq 0$ modes, this correction would be a very difficult task. As demonstrated in Figs. S2 B-S2E, different p modes have different detection efficiencies. And unless one knows the proportion of these p modes a priori, it would not be possible to correct for the coupling efficiencies. Furthermore, even when the OAM spectrum-to-be-measured contains only p=0 modes, it is not possible to implement the correction for more than a few modes. This is because, as discussed above and shown in Figs. S2, an SMF has an appreciable detection efficiency over only a small range of OAM modes. Beyond this range, the signal-to-noise becomes so low that the correction for the coupling efficiency would cause rapidly increasing error in the OAM spectrum estimation with the OAM index.

2 Mode transformation due to mirror reflection

The ket $|l_1, p_1\rangle$ represents the single-photon quantum state with mode indices (l_1, p_1) and $C^{p_1,p_2}_{l_1,l_2}$ is the density matrix element corresponding to indices $((l_1, p_1))$ and $((l_2, p_2))$. The projection of the state $|l_1, p_1\rangle$ on the transverse-polar basis state $|\rho, \phi\rangle$ is given by $\langle\rho, \phi|l_1, p_1\rangle = LG^{|l_1|}_{p_1}(\rho)e^{-il_1\phi}$. As shown in Figure S3 , a mirror reflects an incoming field with azimuthal phase profile $e^{-il\phi}$ and transforms it into $e^{-il(\pi-\phi)}$. Thus, a mirror effectively transforms the state $|\rho, \phi\rangle$ into $|\rho, \pi-\phi\rangle$. This transformation by a mirror can be represented as $\hat{M}|\rho, \phi\rangle = |\rho, \pi-\phi\rangle$,

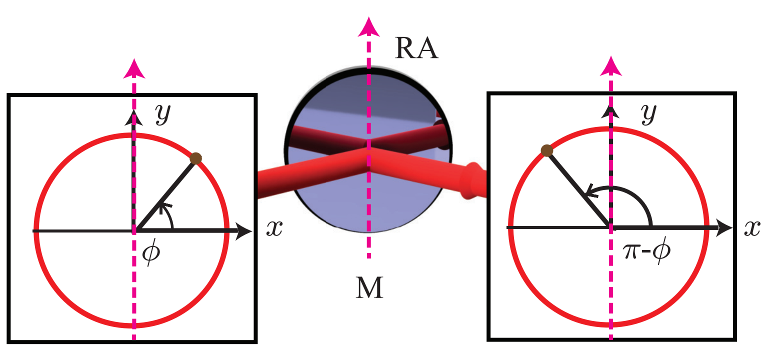

Figure S3: **Mode transformation due to mirror reflection.** An incoming field with transverse phase $e^{il\phi}$ transform into $e^{il(\pi-\phi)}$ through mirror reflection. RA is the reflection axis.

where $\hat{M}$ is the projection operator and can be written as:

$$\begin{aligned}\hat{M} &= \int_0^{\infty}\int_0^{2\pi}\int_0^{\infty}\int_0^{2\pi} |\rho', \phi'\rangle\langle\rho', \phi'|\hat{M}|\rho, \phi\rangle\langle\rho, \phi|\ \rho\rho' d\rho d\rho' d\phi d\phi'. \\ &= \int_0^{\infty}\int_0^{2\pi}\int_0^{\infty}\int_0^{2\pi} |\rho', \phi'\rangle\langle\rho', \phi'|\rho, \pi - \phi\rangle\langle\rho, \phi|\ \rho\rho' d\rho d\rho' d\phi d\phi'. \end{aligned} \tag{S5}$$

Using the inner product $\langle\rho', \phi'|\rho, \pi - \phi\rangle = \frac{1}{\rho}\delta(\rho' - \rho)(\phi' - \pi + \phi)$, we write the projector as

$$\hat{M} = \int_{\rho=0}^{\infty}\int_{\phi=0}^{2\pi} |\rho, \pi - \phi\rangle\langle\rho, \phi|\ \rho d\rho\ d\phi. \tag{S6}$$

Now, using the completeness condition $\sum_{l,p} |l, p\rangle\langle l, p| = \mathbb{I}$, we write $\hat{M}$ in the LG basis as

$$\hat{M} = \sum_{l,p}\sum_{l',p'}\int_{\rho=0}^{\infty}\int_{\phi=0}^{2\pi} |l', p'\rangle\langle l', p'|\rho, \pi - \phi\rangle\langle\rho, \phi|l, p\rangle\langle l, p|\ \rho d\rho\ d\phi. \tag{S7}$$

Next, using the inner product $\langle\rho, \phi|l_1, p_1\rangle = LG_{p_1}^{|l_1|}(\rho)e^{-il_1\phi}$,and performing the integration over ϕ we get

$$\hat{M} = \sum_{l,p}\sum_{l',p'} |l', p'\rangle\langle l, p| \int_{\rho=0}^{\infty}\left[LG_{p'}^{|l'|}(\rho)\right]^* LG_p^{|l|}(\rho)e^{il'\pi}\delta_{l',-l}\ \rho d\rho, \tag{S8}$$

where $\delta_{l',-l}$ is the Kronecker delta. Summing over l' and using the identity $\int_{\rho=0}^{\infty}\left[LG_{p'}^{|l|}(\rho)\right]^* LG_p^{|l|}(\rho)\ \rho d\rho = \delta_{p',p}$, we obtain

$$\hat{M} = \sum_{l,p}\sum_{p'} |-l, p'\rangle\langle l, p|e^{-il\pi}\delta_{p',p}. \tag{S9}$$

Finally, summing over p', we obtain the following expression for the projector:

$$\hat{M} = \sum_{l,p} e^{-il\pi}|-l, p\rangle\langle l, p|. \tag{S10}$$

We find that a reflection transforms the mode $|l, p\rangle$ into mode $|-l, p\rangle\ e^{-il\pi}$. Using the form of $\hat{M}$ above, we can show in a straightforward manner that $\hat{M}^{2n+1} = \hat{M}$ and $\hat{M}^{2n} = \mathbb{I}$, where n is an integer. In other words, an even number of mirrors reflections transforms just as an identity operator whereas an odd number of reflections is equivalent to a single reflection.

3 Mode transformation due to an image rotator

As shown in Fig. S4, an image rotator (IR) when kept at angle θ, transforms the azimuthal phase profile $e^{-il\phi}$ into $e^{-il(\pi+2\theta-\phi)}$. Thus, an image rotator effectively transforms the state $|\rho,\phi\rangle$ into $|\rho,\pi+2\theta-\phi\rangle$. This transformation by an IR can be represented as $\hat{\mathrm{IR}}(\theta)|\rho,\phi\rangle = |\rho,\pi+2\theta-\phi\rangle$, where $\hat{\mathrm{IR}}(\theta)$ is the projection operator. Using the similar procedure as worked out in Section 2, we can write $\hat{\mathrm{IR}}(\theta)$ as:

$$\hat{\mathrm{IR}}(\theta) = \int_{\rho=0}^{\infty}\int_{\phi=0}^{2\pi} |\rho,\pi+2\theta-\phi\rangle\langle\rho,\phi|\, \rho d\rho\, d\phi. \tag{S11}$$

Now, using the completeness condition $\sum_{l,p}|l,p\rangle\langle l,p| = \mathbb{I}$, we write $\hat{\mathrm{IR}}(\theta)$ in the LG basis as

$$\hat{\mathrm{IR}}(\theta) = \sum_{l,p}\sum_{l',p'}\int_{\rho=0}^{\infty}\int_{\phi=0}^{2\pi} |l',p'\rangle\langle l',p'|\rho,\pi+2\theta-\phi\rangle\langle\rho,\phi|l,p\rangle\langle l,p|\, \rho d\rho\, d\phi. \tag{S12}$$

Next, using the inner product $\langle\rho,\phi|l_1,p_1\rangle = LG_{p_1}^{|l_1|}(\rho)e^{-il_1\phi}$, and performing the integration over ϕ we get

$$\hat{\mathrm{IR}}(\theta) = \sum_{l,p}\sum_{l',p'}|l',p'\rangle\langle l,p|\int_{\rho=0}^{\infty}\left[LG_{p'}^{|l'|}(\rho)\right]^{*} LG_{p}^{|l|}(\rho)e^{il'(\pi+2\theta)}\delta_{l',-l}\, \rho d\rho. \tag{S13}$$

where $\delta_{l',-l}$ is the Kronecker delta. Finally, summing over l', using the identity $\int_{\rho=0}^{\infty}\left[LG_{p'}^{|l|}(\rho)\right]^{*} LG_{p}^{|l|}(\rho)\, \rho d\rho = \delta_{p',p}$, and then summing over p', we obtain

$$\hat{\mathrm{IR}}(\theta) = \sum_{l,p} e^{-il(\pi+2\theta)}|-l,p\rangle\langle l,p|. \tag{S14}$$

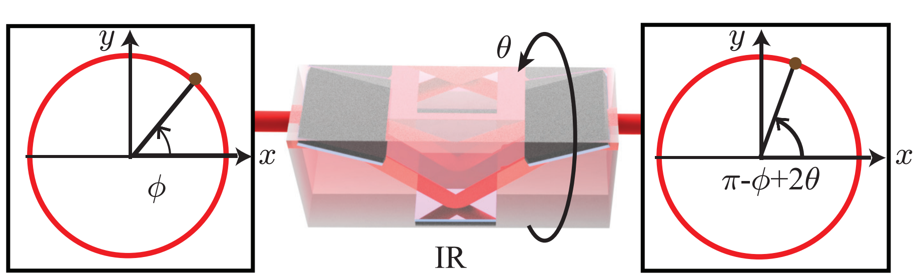

Figure S4: **Mode transformation due to the rotation caused by an image rotator(IR) orientated at angle θ.** An incoming field with the phase profile $e^{il\phi}$ gets transformed into a field having the phase profile $e^{il(\pi-\phi+2\theta)}$.

Thus, an image rotator transforms the mode $|l,p\rangle$ into mode $|-l,p\rangle e^{-il(\pi+2\theta)}$.

4 Derivation of the difference probability

We consider the interferometric setup shown in Fig. 1C of the main text. The input state in the OAM basis is given by the density matrix:

$$\rho_{\text{in}} = \sum_{l_1,l_2=-N}^{+N} \sum_{p_1,p_2=0}^{\infty} C_{l_1,l_2}^{p_1,p_2} |l_1,p_1\rangle\langle l_2,p_2|. \tag{S15}$$

In this interferometer, there are two alternative ways in which an input mode $|l,p\rangle$ can reach the EMCCD plane. One is through the upper arm of the interferometer and second is through the lower arm containing the image rotator. We take the input field to be $\hat{\boldsymbol{x}}$ polarized. In going through the upper arm, an input mode $|l,p\rangle$ faces an odd number of reflections and therefore transforms as

$$|l,p\rangle\hat{\boldsymbol{x}} \rightarrow |-l,p\rangle k_1 e^{-il\pi} e^{i(\beta_1-\omega_0 t_1)}\hat{\boldsymbol{x}}. \tag{S16}$$

In going through the lower arm, the mode faces an even number of reflections and transmits through an image rotator kept at angle θ, therefore, it transforms as

$$|l,p\rangle\hat{\boldsymbol{x}} \rightarrow |-l,p\rangle k_2 e^{-il(\pi+2\theta)} e^{i(\beta_2-\omega_0 t_2)}\hat{\boldsymbol{\epsilon}}(\theta). \tag{S17}$$

Here, ω_0 is the central frequency, and k_1 and k_2 are the fractions of the incoming field passing through the two arms of the interferometer that depend on the reflection and the transmission coefficients of the beam splitters and mirrors; t_1 and t_2 are the photon travel times through the two arms, and β_1 and β_2 are the non-dynamical phases in the two arms. We note that when a mode with the state of polarization $\hat{\boldsymbol{x}}$ passes through an IR rotated at θ, the state of polarization $\hat{\boldsymbol{\epsilon}}(\theta)$ of the transmitted field is given by *(53)*.

$$\hat{\boldsymbol{\epsilon}}\left(\theta\right) = \cos\left[\psi\left(\theta\right)\right]\hat{\boldsymbol{x}} + \sin\left[\psi\left(\theta\right)\right] e^{i\chi(\theta)}\hat{\boldsymbol{y}}, \tag{S18}$$

where $\psi(\theta)$ and $\chi(\theta)$ represent the azimuth and ellipticity of the transmitted field. Using Eqs. (S16) and (S17), we find that an input mode $|l,p\rangle$ in its passage through the interferometer gets transformed as

$$|l,p\rangle\hat{\boldsymbol{x}} \rightarrow |-l,p\rangle k_1 e^{-il\pi} e^{i(\beta_1-\omega_0 t_1)}\hat{\boldsymbol{x}} + |-l,p\rangle k_2 e^{-il(\pi+2\theta)} e^{i(\beta_2-\omega_0 t_2)}\hat{\boldsymbol{\epsilon}}(\theta). \tag{S19}$$

This transformation by the interferometer can be represented by the projection operator $\hat{P}$:

$$\hat{P} = \sum_{l=-\infty}^{\infty}\sum_{p=0}^{\infty} e^{i(-l\pi+\beta_1-\omega_0 t_1+\gamma_1)}\left[|k_1|\hat{\boldsymbol{x}} + |k_2|e^{-i(\delta+2l\theta)}\,\hat{\boldsymbol{\epsilon}}\left(\theta\right)\right]|-l,p\rangle\langle l,p|, \tag{S20}$$

where we have substituted $k_1 = |k_1|e^{i\gamma_1}$, $k_2 = |k_2|e^{i\gamma_2}$ and $\delta = (\beta_1-\beta_2)-\omega_0(t_1-t_2)+\gamma_1-\gamma_2$. In order to modify δ, the upper arm of the interferometer has a geometric phase unit comprising of a quarter-wave plate (Q) with its first axis at $45°$, a half-wave plate (H) with its first axis at $\frac{\delta}{2}$, and an additional quarter-wave plate with its fast axis at $45°$. In terms of the projection operator $\hat{P}$, the output state $\rho_{\rm out}$ corresponding to the input state $\rho_{\rm in}$ in Eq. (S15) is given by

$$\rho_{\rm out} = \hat{P}\rho_{\rm in}\hat{P}^{\dagger}. \tag{S21}$$

Therefore, the total single-photon detection probability $I^{\delta}_{\rm out}(\theta)$ at the EMCCD plane as a function of θ is given by

$$I^{\delta}_{\rm out}(\theta) = \int_0^{\infty}\int_0^{2\pi}\langle\rho,\phi|\rho_{\rm out}|\rho,\phi\rangle\;\rho d\rho\;d\phi = \int_0^{\infty}\int_0^{2\pi}\langle\rho,\phi|\hat{P}\rho_{\rm in}\hat{P}^{\dagger}|\rho,\phi\rangle\;\rho d\rho\;d\phi. \tag{S22}$$

Using Eqs. (S15), (S20) and (S21) and applying the vector relations $\hat{\boldsymbol{x}}\cdot\hat{\boldsymbol{x}} = \hat{\boldsymbol{y}}\cdot\hat{\boldsymbol{y}} = 1$ and $\hat{\boldsymbol{x}}\cdot\hat{\boldsymbol{y}} = 0$, we express $I^{\delta}_{\rm out}(\theta)$ as

$$\begin{aligned} I^{\delta}_{\rm out}(\theta) = &\sum_{l_1,l_2=-N}^{N}\sum_{p_1,p_2=0}^{\infty} C^{p_1,p_2}_{l_1,l_2} e^{i(l_2-l_1)\pi}\left[|k_1|^2 + |k_2|^2 e^{i2(l_2-l_1)\theta}\right. \\ &\left.+|k_1||k_2|\cos\left[\psi\left(\theta\right)\right]\left\{e^{i(\delta+2l_2\theta)} + e^{-i(\delta+2l_1\theta)}\right\}\right]\int_0^{\infty}\int_0^{2\pi}\langle\rho,\phi|-l_1,p_1\rangle\langle -l_2,p_2|\rho,\phi\rangle\rho d\rho\;d\phi. \end{aligned} \tag{S23}$$

Now, using the identity $\int_0^\infty \int_0^{2\pi} \left[LG_{p_1}^{|l_1|}(\rho)e^{-il_1\phi}\right]^* \left[LG_{p_2}^{|l_2|}(\rho)e^{-il_2\phi}\right] \rho d\rho \, d\phi = \delta_{l_1,l_2}\delta_{p_1,p_2}$, we write $I_{\text{out}}^{\delta}(\theta)$ as

$$I_{\text{out}}^{\delta}(\theta) = \sum_{l=-N}^{N} \sum_{p=0}^{\infty} C_{l,l}^{p,p} \left[|k_1|^2 + |k_2|^2 + 2|k_1||k_2| \cos\left[\psi\left(\theta\right)\right] \cos\left(\delta + 2l\theta\right)\right], \tag{S24}$$

The spectrum S_l of an OAM mode with index l is the detection probabilities summed over all the radial modes p having the same OAM index l, that is, $S_l = \sum_{p=0}^{\infty} C_{l,l}^{p,p}$. Thus we write $I_{\text{out}}^{\delta}(\theta)$ as

$$I_{\text{out}}^{\delta}(\theta) = |k_1|^2 + |k_2|^2 + 2|k_1||k_2| \cos\left[\psi\left(\theta\right)\right] \sum_{l=-N}^{+N} S_l \cos(\delta + 2l\theta). \tag{S25}$$

The normalization of the spectrum implies $\sum_{l=-N}^{+N} S_l = 1$. Equation (S25) depicts the total probability at the output of the interferometer due to the input state ρ_{in}. Nonetheless, in realistic experimental situations, the measured probability always contain some noise component $I_n^{\delta}(\theta)$. In our experiments, the main source of noise is from the EMCCD detection. This is due to the fact that of the entire EMCCED camera pixels, only a small portion are involved in detection. These camera pixels are the ones that contribute to the signal. The remaining pixels contribute mostly to the noise because of the inherent dark counts of the EMCCD pixels. The other source of noise include ambient light, etc. Therefore, the measured probability $\bar{I}_{\text{out}}^{\delta}(\theta)$ at the camera plane can be written as

$$\bar{I}_{\text{out}}^{\delta}(\theta) = I_n^{\delta}(\theta) + |k_1|^2 + |k_2|^2 + 2|k_1||k_2| \cos\left[\psi\left(\theta\right)\right] \sum_{l=-N}^{+N} S_l \cos(\delta + 2l\theta). \tag{S26}$$

In order to bypass the effects due to noise sources, we use the two-shot technique *(35)*. We take two probability measurements, one at $\delta = \delta_c$ and the other at $\delta = \delta_d$. Assuming that the shot-to-shot noise remains constant, that is, $I_n^{\delta_c}(\theta) \approx I_n^{\delta_d}(\theta)$, we write the difference probability $\Delta\bar{I}_{\text{out}}(\theta) = \bar{I}_{\text{out}}^{\delta_c}(\theta) - \bar{I}_{\text{out}}^{\delta_d}(\theta)$ as

$$\Delta\bar{I}_{\text{out}}(\theta) = 2|k_1||k_2| \cos\left[\psi\left(\theta\right)\right] \sum_{l=-N}^{+N} S_l[(\cos\delta_c - \cos\delta_d)\cos 2l\theta - (\sin\delta_c - \sin\delta_d)\sin 2l\theta]. \tag{S27}$$

We assume that the spectrum is symmetric, that is, $S_l = S_{-l}$. Therefore $\cos(-2l\theta) = \cos(2l\theta)$, and $\sin(-2l\theta) = -\sin(2l\theta)$. The difference probability $\Delta\bar{I}_{\text{out}}(\theta)$ can now be written as

$$\Delta\bar{I}_{\text{out}}(\theta) = 2|k_1||k_2|\cos\left[\psi\left(\theta\right)\right]\sum_{l=-N}^{N} S_l(\cos\delta_c - \cos\delta_d)\cos 2l\theta. \tag{S28}$$

We note that $\Delta\bar{I}_{\text{out}}(\theta)$ contains the term $\cos\left[\psi\left(\theta\right)\right]$. This is because of the fact that an IR rotates the polarization of incident field. Although it would be ideal to have an image rotator which does not induce any θ-dependent polarization changes, no such image rotator exists currently. Nonetheless, we can bypass this polarization effect by redefining the difference probability as the polarization-corrected difference probability $\Delta I_{\text{out}}(\theta) = \Delta\bar{I}_{\text{out}}(\theta)/\cos\left[\psi\left(\theta\right)\right]$ such that

$$\Delta I_{\text{out}}(\theta) = 2|k_1||k_2|\sum_{l=-N}^{N} S_l(\cos\delta_c - \cos\delta_d)\cos 2l\theta. \tag{S29}$$

We can measure $\cos\left[\psi\left(\theta\right)\right]$ in the following manner. We note that $\cos\left[\psi\left(\theta\right)\right]$ is the projection of the polarization vector along $\hat{\boldsymbol{x}}$. Therefore, $|\cos\left[\psi\left(\theta\right)\right]|^2$ is the ratio of the probability $I_{2x}(\theta)$ along $\hat{\boldsymbol{x}}$-direction and the total probability I_2^{tot}, that is,

$$|\cos\left[\psi\left(\theta\right)\right]|^2 = \frac{|\hat{\epsilon}(\theta)\cdot\hat{\mathbf{x}}|^2}{|\hat{\epsilon}(\theta)|^2} = \frac{I_{2x}(\theta)}{I_2^{\text{tot}}}. \tag{S30}$$

Therefore, $\cos\left[\psi\left(\theta\right)\right] = \sqrt{\frac{I_{2x}(\theta)}{I_2^{\text{tot}}}}$. We note that I_2^{tot} is independent of θ because although an IR rotates the wavefront and polarization, it does not change the probability of the field passing through it. The probabilities I_2^{tot} and $I_{2x}(\theta)$ can be measured by blocking the upper arm of the interferometer. The probability through the IR in this case is I_2^{tot}. For measuring $I_{2x}(\theta)$, one needs to put a polarizer oriented along $\hat{\boldsymbol{x}}$ direction right after the IR and then measure the probability as a function of θ. The polarization corrected difference probability $\Delta I_{\text{out}}(\theta)$ is used for obtaining the OAM spectrum of the input state ρ_{in}.

5 Measurement of non-symmetric OAM spectrum

In this section, we work out how our technique works for an input state ρ_{in} with non-symmetric OAM spectrum, that is, in situation in which the OAM spectrum is not centered around $l = 0$, and $S_l \neq S_{-l}$. Since the assumption $S_l = S_{-l}$ is no longer valid, one cannot measure the spectrum using a two-shot technique. However, we show that it is indeed possible to measure a non-symmetric spectrum in our scheme using a four-shot technique. Unlike in the case of a symmetric spectrum, in which one requires only two intensity measurements at $\delta = 0$ and $\delta = \pi$, a non-symmetric spectrum requires four intensity measurements, one each at $\delta = 0$, $\delta = \pi$, $\delta = \pi/2$ and $\delta = 3\pi/2$. Using equation (S27), we obtain the following expression for the difference probability $\Delta\bar{I}_{\text{out}}^{(0,\pi)}(\theta)$, for $\delta_c = 0$ and $\delta_d = \pi$:

$$\Delta\bar{I}_{\text{out}}^{(0,\pi)}(\theta) = 4|k_1||k_2|\cos\left[\psi(\theta)\right]\sum_{l=-N}^{+N} S_l \cos 2l\theta. \tag{S31}$$

Similarly, taking $\delta_c = 3\pi/2$ and $\delta_d = \pi/2$, and using Eq. (S27), we obtain the following expression for the difference probability $\Delta\bar{I}_{\text{out}}^{(3\pi/2,\pi/2)}(\theta)$:

$$\Delta\bar{I}_{\text{out}}^{(3\pi/2,\pi/2)}(\theta) = 4|k_1||k_2|\cos\left[\psi(\theta)\right]\sum_{l=-N}^{+N} S_l \sin 2l\theta. \tag{S32}$$

Just as in the case of the symmetric spectrum, in order to bypass the effects due to polarization, we work with the polarization corrected difference probabilities $\Delta I_{\text{out}}^{(0,\pi)}(\theta) = \Delta\bar{I}_{\text{out}}^{(0,\pi)}(\theta)/\cos\left[\psi(\theta)\right]$, and $\Delta I_{\text{out}}^{(3\pi/2,\pi/2)} = \Delta\bar{I}_{\text{out}}^{(3\pi/2,\pi/2)}/\cos\left[\psi(\theta)\right]$. Therefore,

$$\Delta I_{\text{out}}^{(0,\pi)}(\theta) = 4|k_1||k_2|\sum_{l=-N}^{+N} S_l \cos 2l\theta$$

$$\Delta I_{\text{out}}^{(3\pi/2,\pi/2)}(\theta) = 4|k_1||k_2|\sum_{l=-N}^{+N} S_l \sin 2l\theta$$

Next, we define the measured OAM spectrum $\bar{S}_l$ as

$$\begin{aligned}\bar{S}_l &\equiv \int_0^{\pi} \left[\Delta I_{\text{out}}^{(0,\pi)}(\theta) + i\Delta I_{\text{out}}^{(3\pi/2,\pi/2)}(\theta)\right] e^{-il2\theta} d\theta \\ &= 4\pi|k_1||k_2| \sum_{l'=-N}^{+N} S_{l'}\delta_{l,l'} \qquad \text{(S33)} \\ &= 4\pi|k_1||k_2| S_l. \qquad \text{(S34)}\end{aligned}$$

Although the measured spectrum $\bar{S}_l$ is not normalized, we find that it is proportional to the true spectrum S_l. Now using the fact that $\text{Tr}\left(\rho_{\text{in}}\right) = 1$, we obtain the true OAM spectrum S_l as

$$S_l = \frac{\bar{S}_l}{\sum_{-N}^{+N} \bar{S}_l}. \qquad \text{(S35)}$$

Thus, one can measure any OAM spectrum S_l using four intensity measurements. In situation in which one has the prior information that the spectrum is symmetric, one can measure the spectrum using only two intensity measurements. Otherwise, using four intensity measurement, one can measure any spectra, symmetric or asymmetric.

6 Effects due to the angular deviation of the image rotator

The accuracy of reconstructing the OAM spectrum through the experimental setup of Fig. 1C of the main text entirely depends on how accurately one is able to measure $\bar{I}_{\text{out}}^{\delta}(\theta)$ of equation (S26) as a function of rotation angle θ. Since $\bar{I}_{\text{out}}^{\delta}(\theta)$ is the intensity due to the interference of the two fields coming through the second beam splitter (BS_2) of Fig. 1C, it is important that the two fields have perfect overlap at the output of the beam splitter (BS_2). Any deviation from the perfect overlap results in error in the measurement of $\bar{I}_{\text{out}}^{\delta}(\theta)$ and thus in the estimated spectrum. However, due to manufacturing issues, IRs invariably introduce angular deviations in the transmitted field and cause the overlap between the two fields to decrease as a fucntion of θ. This is depicted in Figure S5. The field reflecting from (BS_2) is referred to as Beam1 and that

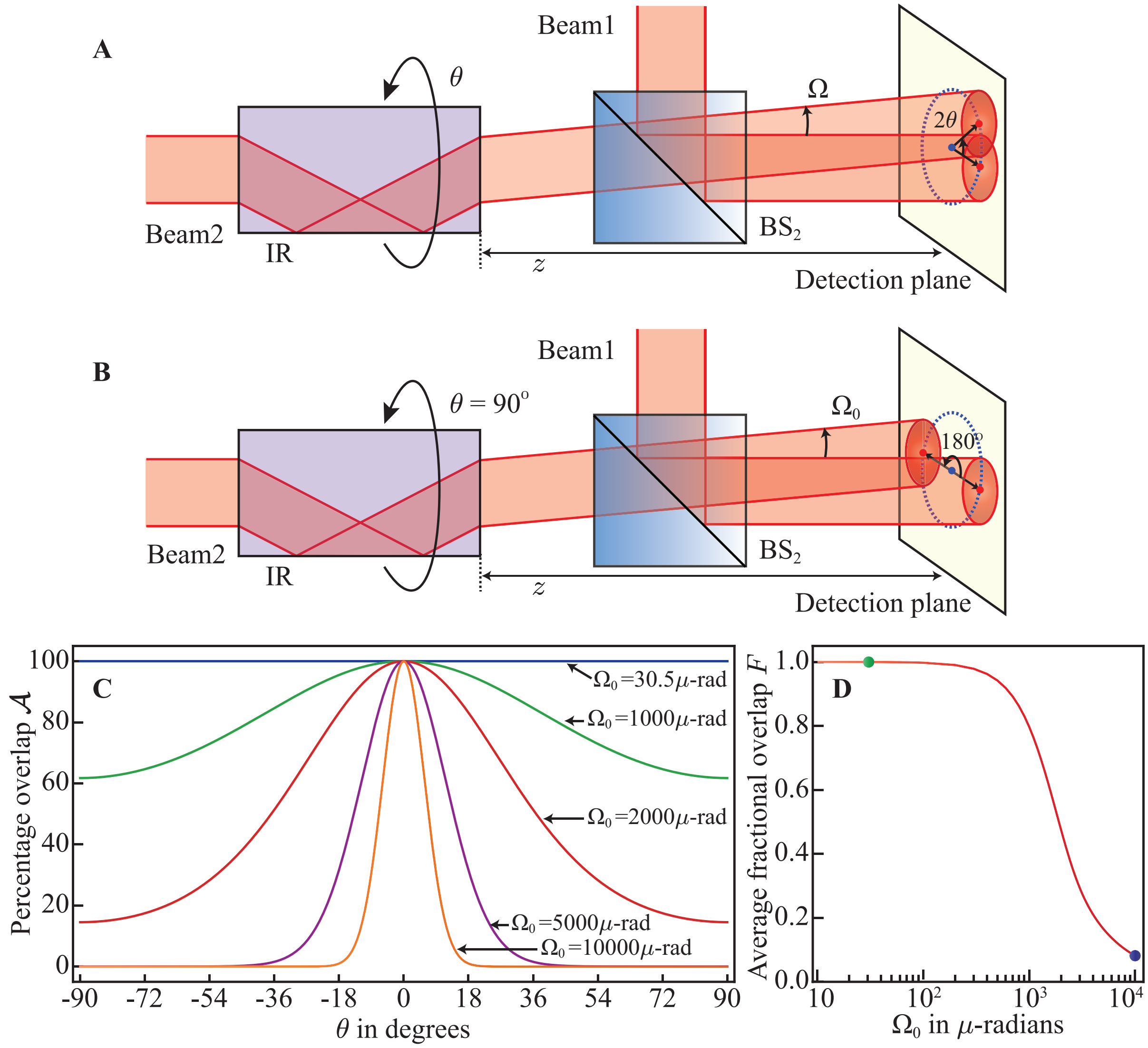

Figure S5: **Conceptual illustration and numerical analysis of the effect of angular deviation of image rotator.** **(A)** Schematic representation of the overlap of Beam1 and Beam2 at the detection plane at a distance z from the image rotator (IR). The angular deviation of Beam2 with respect to Beam1 is defined as Ω. The dotted blue circle traces the trajectory of the center of Beam2 as a function of θ. **(B)** Depiction of the angular deviation at $\theta = 90°$, at which the angular deviation reaches its maximum value Ω_0. **(C)** Plot of percentage overlap $\mathcal{A}$ as a function of θ at five different Ω_0 values. **(D)** The plot of average fractional overlap (F) as a function of Ω_0. $\Omega_0 = 30.5$ μ-radians (green dot) and $\Omega_0 = 10000$ μ-radians (blue dot) correspond to the home-built IR and a typical commercial Dove prism, respectively.

transmitting through it is referred to as Beam2. The detection plane is located at distance z from the IR. When $\theta = 0$, both beams are aligned perfectly with complete overlap at the detection plane. However, as θ increases, rotation of IR causes angular deviation of Beam2 resulting in imperfect overlap as illustrated in Fig. S5A. At $\theta = 90°$, IR introduces maximum angular deviation, represented as Ω_0, resulting in the worst overlap, as shown in Fig. S5B.

In order to numerically analyze this overlap as a function of θ, we first define the center (x_{c2} and y_{c2}) of Beam2 as

$$x_{c2} = z \tan\Omega \left[\cos 2\theta - 1\right], \tag{S36}$$

$$y_{c2} = z \tan\Omega \sin 2\theta. \tag{S37}$$

We note that at $\theta = 0°$, $x_{c2} = 0$ and $y_{c2} = 0$, which implies that Beam1 and Beam2 are perfectly aligned. On the other hand, at $\theta = 90°$, $x_{c2} = -2z\tan\Omega_0$ and $y_{c2} = 0$, and this corresponds to the maximum angular deviation Ω_0. Next, we represent the electric fields of Beam1 and Beam2 at transverse position (x, y) on the detection plane by $E_1\left(x - x_{c1}, y - y_{c1}\right)$ and $E_2\left(x - x_{c2}, y - y_{c2}\right)$, respectively, and define the percentage overlap $\mathcal{A}$ of the two fields as

$$\mathcal{A} = \frac{|\iint E_1\left(x - x_{c1}, y - y_{c1}\right) E_2^*\left(x - x_{c2}, y - y_{c2}\right) dxdy|^2}{\iint |E_1\left(x - x_{c1}, y - y_{c1}\right)|^2 dxdy \iint |E_2\left(x - x_{c2}, y - y_{c2}\right)|^2 dxdy} \times 100\%. \tag{S38}$$

We numerically evaluate $\mathcal{A}$ as a function of θ for five different Ω_0 and plot them in Fig. S5C. The distance to the detection plane is taken to be $z = 250$mm. We find that, for $\Omega_0 = 10000\mu$-radians, which is typically observed with commercial Dove prisms, the overlap $\mathcal{A}$ becomes zero within an angular rotation of about $\pm 18°$. However, for $\Omega_0 = 30\mu$-radians, which is what is achieved with our home-built IR, the overlap $\mathcal{A}$ remains almost constant over the entire range of θ. The percentage overlap $\mathcal{A}$ over the entire range decides how accurately the interferometer is able to measure $\bar{I}_{\rm out}^{\delta}(\theta)$. We quantify this in terms of average fractional overlap (F) under the $\mathcal{A}$ versus θ curve. The fraction is defined by taking $F = 1$ at $\Omega_0 = 0$. We numerically evaluate

F as a function of Ω_0 and plot it in Fig. S5D. We note that at $\Omega_0 = 10000\mu$-radians, represented by the blue dot, that is typically observed with commercial Dove prism, the average fractional overlap $F = 0.0817$. This clearly shows why commercial Dove prism cannot yield accurate estimation of $\bar{I}^{\delta}_{\rm out}(\theta)$ and thus of the OAM spectrum. On the other hand, at $\Omega_0 = 30\mu$-radians, which is shown by the green dot and which corresponds to our home-built IR, the average fractional overlap $F = 0.9998 \approx 1$, implying close to perfect estimation of $\bar{I}^{\delta}_{\rm out}(\theta)$ resulting in near perfect reconstruction fidelity of the OAM spectrum reported in our experiments.

We note that the above analysis is for a detection scheme that assumes no prior knowledge of the input OAM spectrum. However, with prior knowledge, the inaccuracies caused by the angular deviation of image rotators could be bypassed to the extent that one has the prior information.